Visual
Abstract

Finite Fracture Mechanics and Cohesive Crack Model: Size effects through a unified formulation

F. Ferrian, P. Cornetti

Department of Structural, Building and Geotechnical Engineering, Politecnico di Torino, Corso Duca degli Abruzzi 24, 10129 Torino, Italy.
francesco.ferrian@polito.it; https://orcid.org/0000-0002-2093-5765
pietro.cornetti@polito.it; https://orcid.org/0000-0001-9063-9913

L. Marsavina

Department of Mechanics and Strength of Materials, University Politehnica Timisoara, Blvd. M. Viteazu, No. 1, 300222 Timisoara, Romania.
liviu.marsavina@upt.ro; https://orcid.org/0000-0002-5924-0821

A. Sapora

Department of Structural, Building and Geotechnical Engineering, Politecnico di Torino, Corso Duca degli Abruzzi 24, 10129 Torino, Italy.
alberto.sapora@polito.it; https://orcid.org/0000-0003-3181-3381

ABSTRACT. Finite Fracture Mechanics and Cohesive Crack Model can effectively predict the strength of plain, cracked or notched structural components, overcoming the classical drawbacks of Linear Elastic Fracture Mechanics. Aim of the present work is to investigate size effects by expressing each model as a unified system of two equations, describing a stress requirement and the energy balance, respectively. Brittle crack onset in two different structural configurations is considered: (i) a circular hole in a tensile slab; (ii) an un-notched beam under pure bending. The study is performed through a semi-analytical parametric approach. Finally, theoretical strength predictions are validated with experimental results available in the literature for both geometries, and with estimations by the point criterion in the framework of Theory of Critical Distances.

KEYWORDS. Size effects; Finite Fracture Mechanics; Cohesive Crack Model; Circular hole; Pure bending; crack advance.

INTRODUCTION

Since the pioneering work by Hillerborg et al. 1976 [1] the Cohesive Crack Model (CCM) has been widely implemented to assess the failure behavior of plain or composite structural components (e.g., [2]). The approach is based on the definition of a constitutive relationship, linking the cohesive stresses acting on the process zone with the crack lip opening displacement. CCM can provide physically-based and accurate strength estimations, but usually at the price of huge computational efforts.

On the contrary, as regards the brittle crack onset, the coupled Finite Fracture Mechanics (FFM) criterion [3, 4] allows to achieve (semi-) analytical predictions, thus generally revealing a more efficient approach. It relies on the assumption of a finite crack increment (at least at the first step), and it involves the fulfilment of two conditions: a stress requirement and the energetic balance.

CCM and FFM predictions were compared for different notched configurations, from V-notches [5-7] to cracks [8, 9], fiber-matrix debonding [10] and spherical voids [11]. The above studies show that FFM and CCM can lead to very close predictions, depending on the FFM stress condition, the CCM constitutive law and the structural configuration under investigation. Note that in [11] the CCM was written explicitly as a system of two equations, representing a stress-based condition and an energy requirement, thus rendering straightforward the analogy with FFM. In this context, the process zone can be thought as the CCM's counterpart of the finite crack propagation distance. Therefore, up to a certain extent, both FFM and CCM are equivalent in terms of the quantities they both rely on to predict the crack nucleation. Furthermore, for cracked geometries, both models describe the transition from a strength-governed failure to a toughness-governed one as the size increases, unlike what happens with Linear Elastic Fracture Mechanics (LEFM), which is not able to catch this transition.

Aim of this paper is to extend the comparison between CCM and FFM to other two configurations: (i) a circular hole in a tensile slab; (ii) an un-notched slender beam under four point bending (FPB). The former geometry was already addressed numerically by both CCM and FFM in Li et al. [12], whereas the latter was recently investigated through FFM by Doitrand et al. [13]. The novelty here relies on the proposed unified approach for each model, the analytical relationships governing the two problems being formally the same, up to the shape functions involved.

The study will be carried out assuming a Dugdale law for CCM (Fig. 1) and the original version of FFM (Leguillon [3]). Finally, to corroborate the theoretical results, experimental data from the literature on materials implemented in different engineering fields will be taken into account, revealing a general good agreement. Predictions by the point criterion in the framework of Theory of Critical Distances [14] will be also reported.

THEORETICAL APPROACHES

The coupled FFM criterion and the CCM will be introduced below by referring to mode I loading conditions (Fig.2), coherently with the topic under investigation.

Finite Fracture Mechanics

According to coupled FFM approaches [3], [15], a stress and an energy requirements have to be simultaneously fulfilled for brittle crack onset to take place. The stress condition, following Leguillon's approach [3], requires that the normal stress σ_y over a finite distance Δ must be larger than the ultimate tensile strength σ_c of the material. On the other hand, the energy balance imposes that the strain energy G available for the finite crack increment Δ must be greater than $G_c\Delta$, where G_c is the material fracture energy. Coupling the two conditions above, a system of two inequalities is obtained:

$$\begin{cases} \sigma_y(x) \geq \sigma_c & 0 \leq x \leq \Delta \\ \int_0^\Delta G(a)\,\mathrm{d}a \geq G_c\Delta \end{cases} \tag{1}$$

According to FFM, the actual failure load is the minimum one satisfying the two inequalities (1). However, for a positive geometry (i.e. for a monotonically increasing strain energy release rate along the crack length) the failure load is achieved when the two inequalities are strictly verified. In this case, Eqn. (1) reverts to a system of two equations, see Eqn. (2): note that the energy balance has been rewritten through Irwin's relationship, thus introducing the stress intensity factor $K_I = \sqrt{}$

(GE') and the material fracture toughness $K_{IC} = \sqrt{(G_c E')}$, E' being the Young's modulus under plain strain conditions. The two unknowns are represented by the critical (failure) stress σ_f, implicitly embedded in the stress field and the SIF functions, and the critical crack increment Δ_c. This latter quantity results a structural parameter, since dependent on both material properties and geometric characteristics. The behavior will be addressed more in details in Section 3.

$$\begin{cases} \sigma_y(\Delta_c) = \sigma_c \\ \int_0^{\Delta_c} K_I{}^2(a)\,\mathrm{d}a = K_{IC}{}^2 \Delta_c \end{cases} \tag{2}$$

Considering just the former equation of system (2), the Point Method (PM) can be defined [14, 16]. According to this criterion, fracture takes place when the stress equals the tensile strength σ_c at a critical distance $\Delta_c = l_{ch} / (2\pi)$, where $l_{ch} = (K_{IC} / \sigma_c)^2$ is the well-known Irwin's length. Thus, according to TCD, the crack advance is a material property.

Cohesive Crack Model
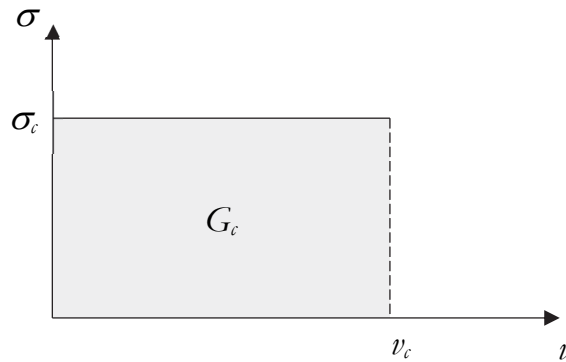Let us now consider the CCM implementing a Dugdale type cohesive law (Fig. 1).

Figure 1: Dugdale's cohesive law.

According to this model, a process zone of length a_p is present ahead the crack/notch tip, where the cohesive stress keeps constant and equal to σ_c: a_p increases with the external load σ, finally reaching the critical value a_{pc} when σ is maximum, i.e. $\sigma = \sigma_f$. To achieve a_{pc} and σ_f, two different conditions must be considered. The former is a stress requirement: the global SIF K_I has to vanish at the fictitious crack tip, such to eliminate the stress singularity. The superposition principle allows to exploit the SIFs due to the external loading $K_{I\sigma}$ and the cohesive stresses $K_{I\sigma_c}$, so that:

$$K_I = K_{I\sigma} - K_{I\sigma_c} = 0 \tag{3}$$

The latter is an energy condition: crack nucleates when the crack tip opening displacement (CTOD) v attains its critical value $v_c = G_c / \sigma_c$. In formulae, thanks again to superposition:

$$v = v_\sigma - v_{\sigma_c} = v_c \tag{4}$$

where v_σ and v_{σ_c} are the CTODs related, respectively, to σ and σ_c. They can be computed by a straightforward application of Paris' equation as:

$$v_\sigma = \frac{2}{E'} \int_0^{a_p} K_{I\sigma}(\sigma, a) \frac{\partial K_{IP}(P, a)}{\partial P}\,\mathrm{d}a \tag{5}$$

$$v_{\sigma_c} = \frac{2}{E'} \int_0^{a_p} K_{I\sigma_c}(\sigma_c, a) \frac{\partial K_{IP}(P, a)}{\partial P}\,\mathrm{d}a \tag{6}$$

In Eqns. (5) and (6) K_{IP} is the SIF related to a pair of normal forces P, per unit of thickness, acting at the crack onset point (see Appendix A for a graphical representation).

TEST GEOMETRIES

Two different geometries are here analyzed. The first one is a circular hole with radius c in an infinite slab under uniaxial tensile load σ. The geometry and the system of reference taken into account are represented in Fig. 2(a). Note that the study concerns symmetrical crack propagation (i.e. two cracks simultaneously stemming from the hole edge) according to what presented in [17]. As will be clear later, the analysis can be easily extended to a finite geometries by properly taking some multiplying corrections factors into account.
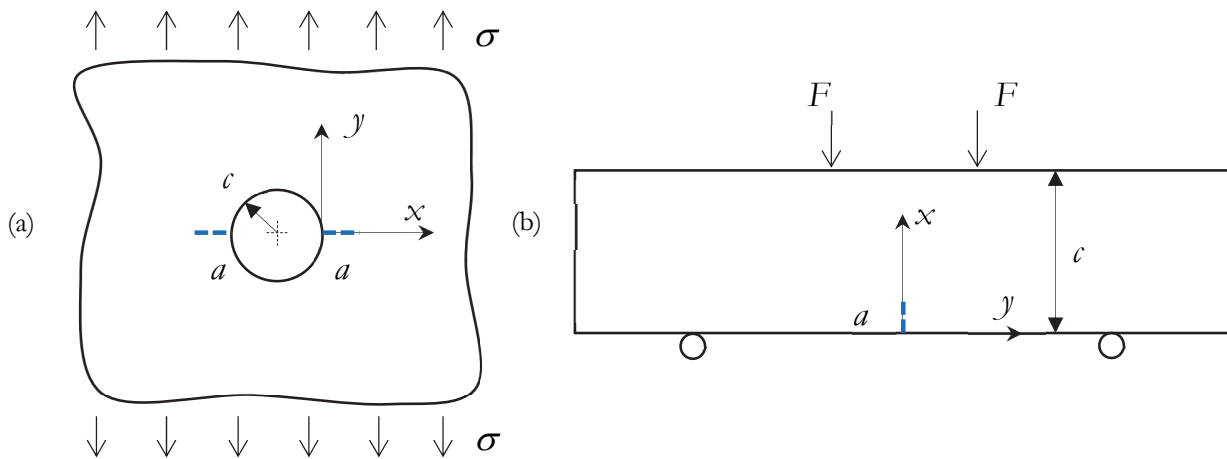

Figure 2: (a) Circular hole in an infinite tensile plate and (b) FPB configuration.

The second one is a sufficiently slender beam of height c loaded under four point bending (FPB, Fig. 2(b)). This configuration generates a state of pure bending in the middle section of the beam, i.e. where fracture is supposed to take place.

The normal stress field along the x axis can be expressed as:

$$\sigma_y\left(\overline{x}\right) = f_\sigma\left(\overline{x}\right)\sigma \tag{7}$$

where $\overline{x} = x / c$ is the dimensionless coordinate and $\sigma = \sigma_{max} = 6M / c^2$ for the FPB geometry (M being the bending moment). The (exact) analytical functions $f_\sigma\left(\overline{x}\right)$ according to Kirsch [18] and beam theory are reported in Appendix A.

Note that for the holed configuration, Eqn. (7) provides the well-known stress concentration factor $K_t^\infty = 3$ at the hole edge ($\overline{x} = 0$), whilst far from the hole the stress field tends to the applied stress σ.

On the other hand, the SIF related to crack initiation (Fig. 2) can be put in the following form:

$$K_{I\sigma} = \sigma\sqrt{\pi a}F_\sigma\left(\overline{a}\right) \tag{8}$$

where $\overline{a} = a / c$.

Eqns. (7) and (8) are sufficient to apply FFM. Moreover, the expression for $K_{I\sigma_c}$ (Eqn. (3)) and K_{IP} (Eqns. (5,6)) necessary to implement the CCM can be expressed, respectively, by the following relationships:

$$K_{I\sigma_c} = \sigma_c\sqrt{\pi a}F_{\sigma_c}\left(\overline{a}\right) \tag{9}$$

$$K_{IP} = \frac{P}{\sqrt{\pi a}} F_P(\overline{a}) \tag{10}$$

The approximating shape functions $F_{\sigma}(\overline{a})$, $F_{\sigma_c}(\overline{a})$, $F_p(\overline{a})$ and their respective accuracy are reported in Appendix A for both geometries.

FFM and CCM results
Considering the equations provided for the two geometries analyzed in Section 3, FFM and CCM can now be implemented. As concerns FFM, introducing the expression for σ_y provided by Eqn. (7) and for $K_{I\sigma}$ given by Eqn. (8) into Eqn. (2), yields:

$$\begin{cases} \dfrac{\sigma_f}{\sigma_c} = \dfrac{1}{f_{\sigma}(\overline{\Delta}_c)} \\[3mm] \gamma = \dfrac{\overline{\Delta}_c}{\pi} \dfrac{f_{\sigma}^2(\overline{\Delta}_c)}{\int_0^{\overline{\Delta}_c} \overline{a} \, F_{\sigma}^2(\overline{a}) \, d\overline{a}} \end{cases} \tag{11}$$

where $\overline{\Delta}_c = \Delta_c / c$ and $\gamma = c / l_{ch}$.

Thus, the size effect law according to FFM can be investigated as a parametric curve where the dimensionless size γ and failure stress σ_f / σ_c are both expressed as a function of $\overline{\Delta}_c$.

On the other hand, as regards CCM, substituting the expressions of $K_{I\sigma}$ (Eqn. (8)) and $K_{I\sigma_c}$ (Eqn. (9)) into Eqn. (3), yields:

$$\sigma\sqrt{\pi a_p} F_{\sigma}(\overline{a}_p) - \sigma_c \sqrt{\pi a_p} F_{\sigma_c}(\overline{a}_p) = 0 \tag{12}$$

where $\overline{a}_p = a_p / c$ is the dimensionless process zone. In critical conditions, the dimensionless strength σ_f / σ_c as a function of $\overline{a}_{pc}$ can be derived from Eqn. (12). Furthermore, in light of the energy condition (4) and of the CTODs expressions provided by Eqns. (5)-(6), the dimensionless characteristic size γ can be expressed as a function of $\overline{a}_{pc}$ through Eqns. (8-10), leading to:

$$\begin{cases} \dfrac{\sigma_f}{\sigma_c} = \dfrac{F_{\sigma_c}(\overline{a}_{pc})}{F_{\sigma}(\overline{a}_{pc})} \\[3mm] \gamma = \dfrac{1}{2} \left\{ \dfrac{F_{\sigma_c}(\overline{a}_{pc})}{F_{\sigma}(\overline{a}_{pc})} \int_0^{\overline{a}_{pc}} \left[F_{\sigma}(\overline{a}_p) - F_{\sigma_c}(\overline{a}_p) \right] F_P(\overline{a}_p) \, d\overline{a}_p \right\}^{-1} \end{cases} \tag{13}$$

Hence, also CCM consists of a parametric approach, where the dimensionless size γ and failure stress σ_f / σ_c reveal now functions of $\overline{a}_{pc}$.

As concerns the holed configuration, the failure stress estimations provided by FFM (Eqn. (11)) and CCM (Eqn. (13)) using the shape functions through Eqns. (A1)-(A4), are plotted in Fig. 3. As evident, the theoretical predictions are quite close. The relative deviation increases up to 8 % for $\gamma \approx 8$, and then it decreases as γ increases. In Fig. 3 the experimental data on two different polymeric materials, polymethyl-methacrylate (PMMA) and general-purpose polystyrene (GPPS), tested by Sapora et al. [17], are also reported. The geometry referring to $c / w = 1 / \overline{w} \leq 0.05$ (w being the plate width), the theoretical assumption of an infinite geometry is here validated. The material properties for both PMMA and GPPS are summarized in Tab. 1.

	Reference	K_{IC} [MPa√m]	σ_c [MPa]	l_{ch} [mm]
Concrete	[19]	0.6^	3.8^	24.9
ZnO	[20]	1.27°	100°	0.16
PUR	[21]	1.25	17.4	5.19
GPPS	[17]	1.40	30	2.18
PMMA	[17]	1.96	70.5	0.77
α-gypsum	[13]	0.35+	9.5+	1.36
β-gypsum	[13]	0.10+	2.7+	1.37
γ-gypsum	[13]	0.40+	12+	1.11
UHPFRC	[22]	4.45*	11.5	150

Table 1: Material properties implemented in this study.

^ Material properties are not provided in the reference article and they are estimated based on [23].

° In the reference article the material properties are estimated based on [24].

+ In the reference article the material properties are estimated based on [25], [26], [27].

* K_{IC} is not provided in the reference article. The value is estimated based on [28].

The failure stress predictions provided by CCM and FFM are in fairly good agreement with the experimental results on PMMA. The maximum percent discrepancy from the estimations furnished by the CCM is 9 % for $\gamma \approx 2.6$, whereas it decreases to 6 % for $\gamma \approx 0.65$ according to FFM.

Predictions are also satisfactory for GPPS, even if in this case the discrepancy is higher. Indeed, the maximum deviation from CCM and FFM failure predictions exceeds, respectively, 15 % and 17 % for $\gamma \approx 0.23$.

PM predictions are also depicted in Fig. 3, revealing the most conservative criterion: the maximum percent discrepancy from PMMA experimental data increases up to 17 %, whereas the deviation from GPPS test results decreases to 12 %.
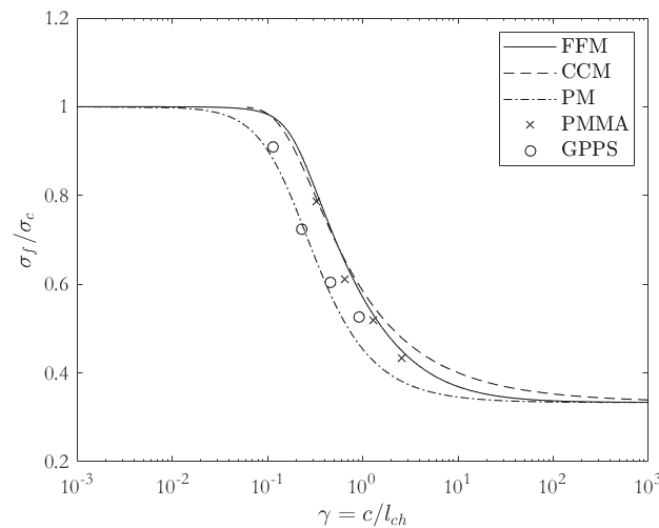

Figure 3: Circular hole in an infinite tensile slab: size effects by FFM (continuous line), CCM (dashed line), PM (dash-dotted line) and experiments on PMMA and GPPS [17].

A third set of experimental data is now considered, to further validate the models. It refers to polyurethane (PUR) tested by Negru et al. [21], see also [29]. In this case the sample width w was equal to 25 mm with variable ratios $c/w = 1/\bar{w}$ ranging from 0.02 to 0.2. Thus, the influence of the finite dimension of the specimens on failure predictions has to be taken into account. To this purpose, we consider the following correction factor for the stress field [30]:

$$m_\sigma^w = \frac{K_t}{K_t^\infty} = \left[\frac{3\left(1 - 2/\overline{w}\right)}{2 + \left(1 - 2/\overline{w}\right)^3} \right]^{-1} \tag{14}$$

where K_t is the stress concentration factor of a finite plate containing a circular hole (whereas $K_t^\infty = 3$): the stress field for finite width plates is achieved by multiplying Kirsch solution (A1) by m_σ^w. The accuracy of the correction provided by m_σ^w was evaluated through a Finite Element Method (FEM) analysis using ANSYS® code. In Fig. 4 it is represented the comparison between K_t and K_t^{FEM}, determined through a convergence analysis, for different ratios $2/\overline{w}$: the two quantities are in good agreement each other and the percent discrepancy is less than 3 % for $2/\overline{w} < 0.4$.
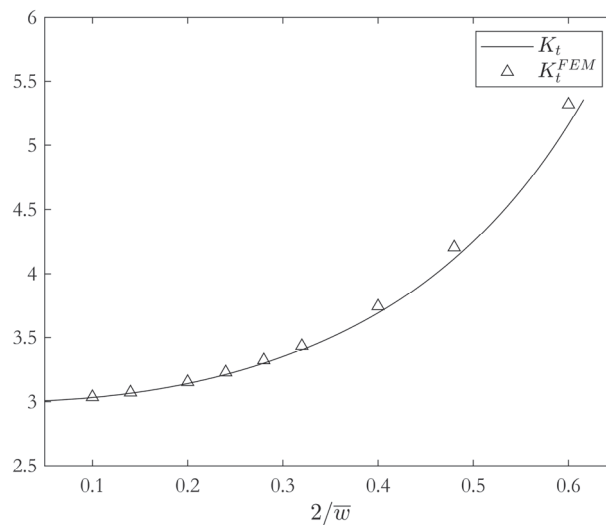

Figure 4: Circular hole in a finite tensile plate: comparison between K_t and K_t^{FEM} for different ratios $2/\overline{w}$.

To implement FFM and CCM we need to estimate also the correction factors for $K_{I\sigma}$ and $K_{I\sigma_c}$ related a finite width geometry. This is accomplished by multiplying Eqns. (8) and (9) by the following correction factors [31], [32]:

$$M_\sigma^w = \sqrt{\sec\left(\frac{\pi}{\overline{w}}\right) \sec\left[\frac{\pi\left(\overline{a} + 1\right)}{\overline{w}}\right]} \tag{15}$$

$$M_{\sigma_c}^w = \frac{\pi/2 - \sin^{-1}\left\{\sin\left(\frac{\pi}{\overline{w}}\right) \Big/ \sin\left[\frac{\pi\left(\overline{a} + 1\right)}{\overline{w}}\right]\right\}}{\pi/2 - \sin^{-1}\left(\frac{1}{\overline{a} + 1}\right)} \tag{16}$$

Eqn. (15) is valid for $2/\overline{w} \leq 0.5$ and $2(c + a)/w \leq 0.7$ and it is between $\pm$ 2 % of boundary-collocation results (Newman Jr [33]). On the other hand, the value of $K_{I\sigma_c}$, for different ratios $2(c+a)/w$, was compared with that determined exploiting the Fracture Tool available in ANSYS® code. The two values are in perfect agreement each other, the deviation was found to be less than 2% for $2(c + a)/w < 0.7$. Details of the mesh and the geometry implemented in the FEM analysis are reported in Fig. 5. Note that, based on [31], Eqns. (15) and (16) can be applied directly even to compute the CTODs, i.e. Eqn. (4) can be implemented, without the necessity of improving Eqns. (5) and (6).
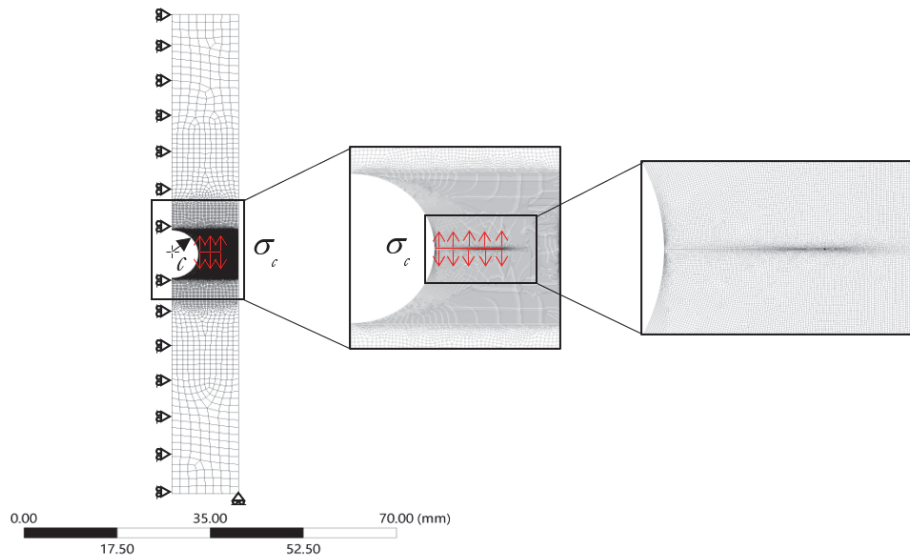
Figure 5: Details of the mesh, constraints and loads used in the FEM model to evaluate the accuracy by Eqn. (16).

The failure stress estimations provided by FFM and CCM for a finite width geometry through Eqns. (14)-(16) are finally plotted in Fig. 6. As clearly highlighted in this figure, CCM and FFM fit well the data, especially for $\gamma > 0.5$. As γ decreases the percent discrepancy increases up to 20 % for $\gamma \approx 0.1$. On the contrary, the accuracy of the PM reveals questionable for this data set, especially for large scale-sizes.
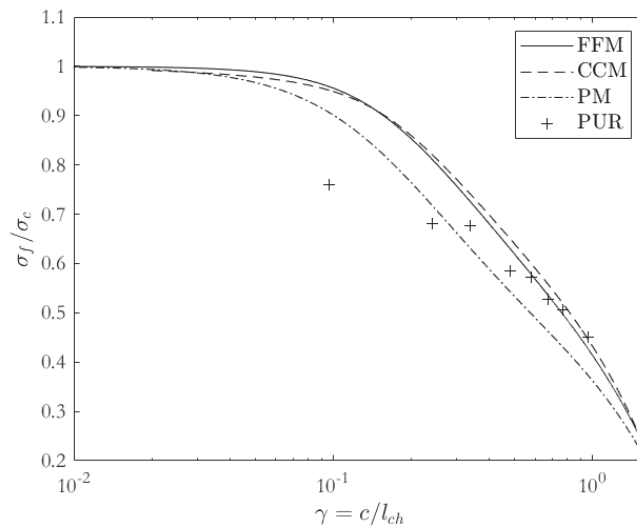

Figure 6: Circular hole in a finite tensile slab: size effects by FFM (continuous line), CCM (dashed line), PM (dash-dotted line) and experiments on PUR [21].

The finite crack advancement Δ_c / l_{ch}, provided by Eqn. (11) multiplying $\bar{\Delta}_c$ with γ, and the process zone length a_{pc}, given similarly by Eqn. (13), are represented in Fig. 7. The absolute values of the two sizes are quite different between each other. Nevertheless, the trend with respect to the dimensionless size γ is somehow similar. Considering FFM, Δ_c decreases from the value $2 \, l_{ch} / \pi$ until it reaches a minimum and then it tends to $2 \, l_{ch} / [\pi(1.12)^2]$ as γ increases. Analogously, a_{pc} decreases until it reaches a minimum for $\gamma \approx 0.4$, and then it increases monotonically. The deviation between the process zone length in CCM and the finite crack advancement in FFM may be explained considering that whereas a_{pc} is a fictitious crack, since cohesive stresses are present, Δ_c is a "real" crack, because the new crack lips are stress free.
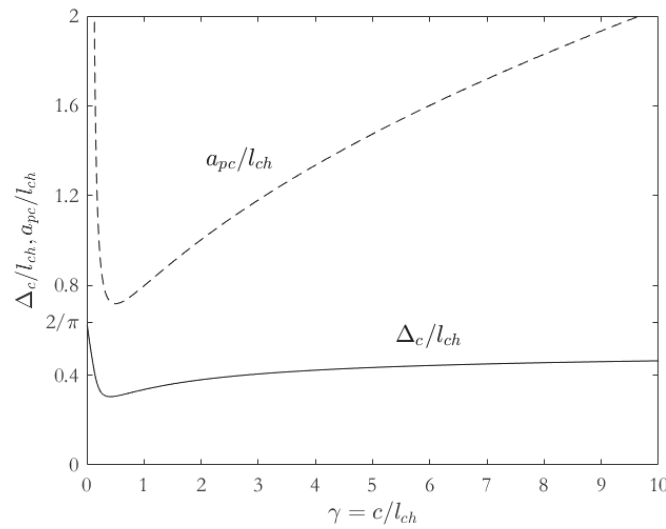
Figure 7: Circular hole in an infinite tensile slab: finite crack extension Δ_c / l_{ch} by FFM (continuous line), process zone length a_{pc} / l_{ch} by CCM (dashed line).

Analyzing now the FPB geometry (Fig. 2(b)), we can apply the shape functions provided by Eqns. (A5)-(A8) to Eqns. (11) and (13) for FFM and CCM, respectively.
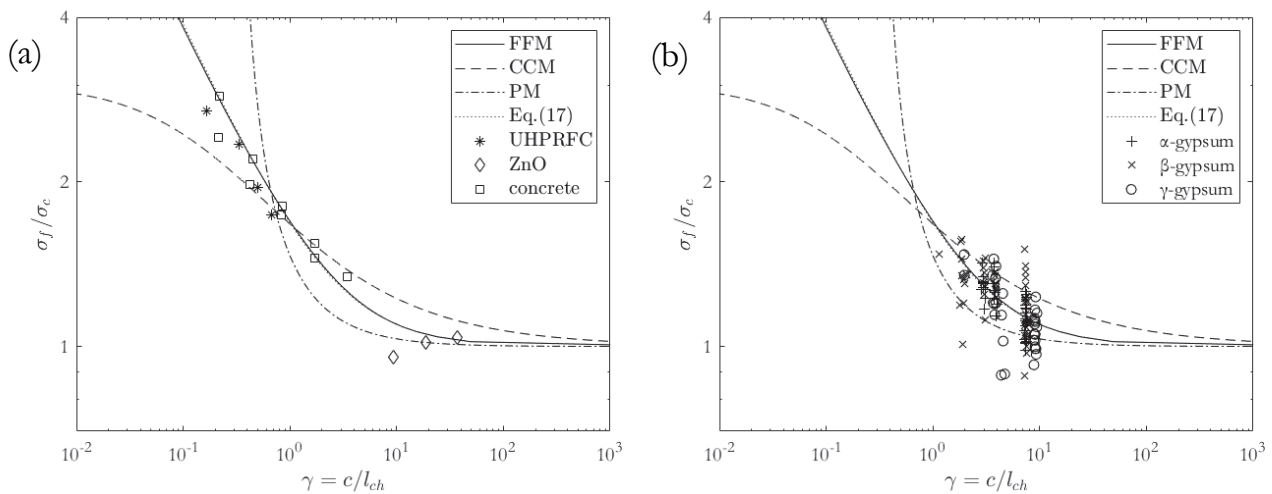

Figure 8: Size effects on FPB un-notched samples: FFM (continuous line), CCM (dashed line), PM (dash-dotted line) and experimental results for (a) UHPFRC [22], ZnO [20] and Concrete [19]; (b) gypsum [13].

The failure stress estimates σ_f is reported in Fig. 8 as a function of the dimensionless characteristic size $\gamma = c / l_{ch}$. The failure stress estimates of the two models are quite different for small-size structures. CCM furnishes a dimensionless small-size limit strength value equal to 3, whereas FFM provides an infinitely large strength for vanishing size (the slope of the curve is equal to 0.5 in the log-log plot). Analogously, PM furnishes the lowest predictions for $\gamma > 0.7$. On the other hand, it provides divergent predictions as γ approaches $1/\pi$, this representing the limit below which stresses (at a distance Δ_c from the beam edge) become negative.

Together with these estimations, in this figure are represented also the experimental data related to three different types of gypsum [13], Ultrahigh-Performance Fiber-Reinforced Concrete (UHPFRC, [22]), Zinc Oxide (ZnO, [20]) and concrete [19]. The material properties considered in this study are again resumed in Tab. 1.

Theoretical predictions are in good agreement with results on gypsum, despite the high statistical dispersion of the experimental data. This scattering can be partially explained considering the presence of critical pores triggering failure, as

highlighted by Uhl et al. [34]. Considering UHPFRC, estimations provided by FFM and CCM are again accurate. Indeed, CCM provides a deviation that increases up to 15 % as γ decreases, whilst FFM furnishes a lower percent discrepancy, equal to 14 % for $\gamma \approx 0.17$. Similar arguments hold for concrete and ZnO data.

Furthermore, also the approximated results provided by Eqn. (17) are represented in Fig. 8: this master curve is in excellent agreement with FFM predictions in the range of practical interest, the percent discrepancy is less than 1.5 % for $\gamma \geq 0.1$. With respect to that proposed in [13], Eqn. (17) is able to catch the FFM trend at small scales, thus revealing more accurate.

$$\frac{\sigma_f}{\sigma_c} = \left(1 + \frac{2.5}{c/l_{ch}}\right)^{\frac{1}{2.4}} \qquad (17)$$

Fig. 9 represents the comparison between the finite crack advance according to FFM and the process zone according to CCM, normalized with respect to Irwin's length. As clearly highlighted in the plot, both models provide curves with slope equal to 1 for vanishing γ (i.e., $a_{pc} = c$ and $\Delta_c = c / 2$). Furthermore, in accordance with CCM, the process zone diverges in large scale limit (linear slope equal to 0.5, $a_{pc} = 0.5\sqrt{(c\, l_{ch})}$), while the crack advance Δ_c tends to $2\, l_{ch} / [\pi(1.12)^2]$, i.e., the same value obtained for the holed configuration.
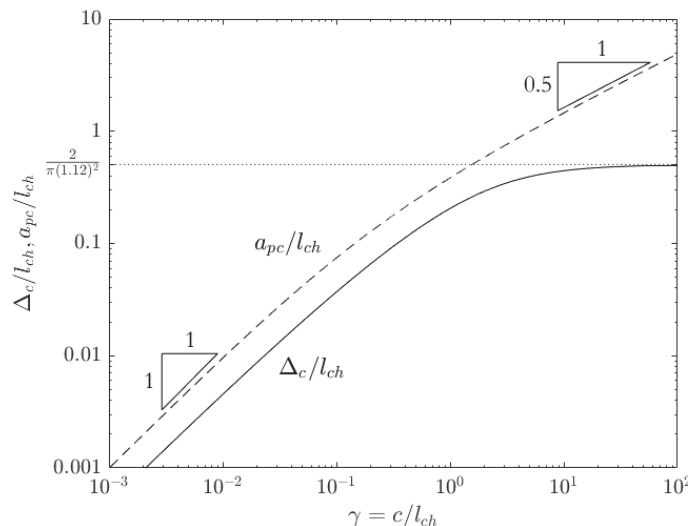

Figure 9: FPB configuration: finite crack extension Δ_c / l_{ch} by FFM (continuous line), process zone length a_{pc} / l_{ch} by CCM (dashed line).

CONCLUSIONS

In the present paper, two different configurations - a tensile strip (or plate) with a circular hole and a FPB un-notched beam- were analyzed to catch size effects implementing FFM and CCM. In order to compare theoretical predictions, a rectangular cohesive law (Dugdale's type) was considered for CCM and a point wise stress requirement was implemented for FFM [3]. The analysis was conducted in a semi-analytical way by exploiting shape functions available in Literature, leading to a unified parametric approach for each model. Note that in the framework of FFM, this had already been done for the three point bending configuration of plain or cracked specimens [4] or dealing with blunt V-notches [35], which can be easily recast according to the present formulation.

For the holed geometry the failure estimations provided by these two approaches are very close to each other. Instead, for the FPB geometry, the dissimilarities between the strength previsions provided by the two approaches increase at smaller scales. Indeed, CCM tends towards a dimensionless strength value equal to 3, whereas FFM provides an infinitely large strength for vanishing sizes. The comparison with experimental data from the literature on different materials shows that FFM is able to catch the correct trend in the region of practical interest, whereas PM -and, generally, each model based on a material length- is not. It is worthwhile remarking, once again, the matching between FFM and CCM, although

consolidated, actually depends on the geometry under investigation, the CCM cohesive law, and the particular FFM stress condition.

APPENDIX A

Circular holed configuration

The function $f_\sigma(\overline{x})$ can be expressed as [18]:

$$f_\sigma\left(\overline{x}\right)=1+\frac{1}{2(\overline{x}+1)^2}+\frac{3}{2(\overline{x}+1)^4}$$

(A1)

The shape functions $F_\sigma(\alpha)$, $F_{\sigma_c}(\alpha)$ according to [36], and $F_P(\alpha)$ provided in [37] can be expressed as (Fig. A1, accuracy of about 1 %):

$$F_\sigma\left(\overline{a}\right)=\frac{1}{2}\frac{3+2\overline{a}}{1+\overline{a}}\left[1+\frac{1.243}{\left(1+\overline{a}\right)^3}\right]$$

(A2)

$$F_{\sigma_c}\left(\overline{a}\right)=\frac{\left(1+\overline{a}\right)^4-0.137\left(1+\overline{a}\right)^3+0.258\left(1+\overline{a}\right)-0.4\overline{a}^2}{\left(1+\overline{a}\right)^4}$$

(A3)

$$F_P\left(\overline{a}\right)=\frac{2\sqrt{1+\overline{a}}}{\sqrt{2+\overline{a}}}\left[1+\frac{0.201}{\left(1+\overline{a}\right)^2}+\frac{0.604}{\left(1+\overline{a}\right)^4}\right]$$
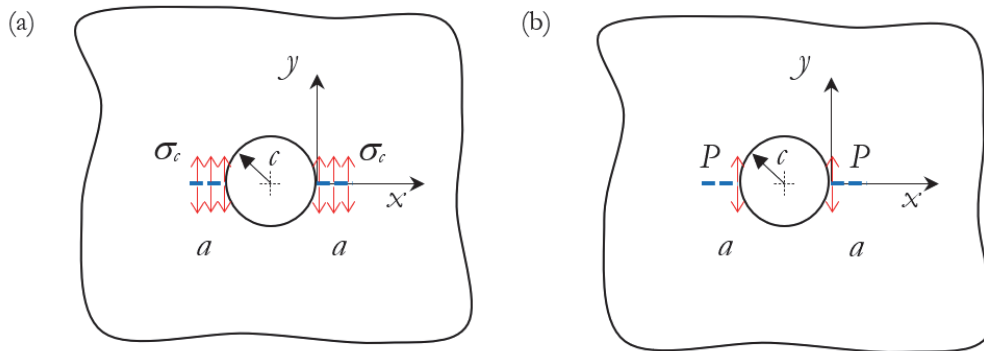
(A4)

Figure A1: Schematic representation of the considered loadings: (a) cohesive stress acting on the crack length *a*; (b) pair of normal forces *P* applied at the hole edge.

FPB un-notched beam

According the elementary beam theory, the function $f_\sigma(\overline{x})$ is given by:

$$f_\sigma\left(\overline{x}\right)=1-2\overline{x}$$

(A5)

For this configuration, the shape functions $F_\sigma(\alpha)$, $F_{\sigma_c}(\alpha)$ and $F_p(\alpha)$ according to [36] (Fig. A2, accuracy less than 0.5 %):

$$F_{\sigma}\left(\overline{a}\right) = \sqrt{\frac{2}{\pi\overline{a}}\tan\left(\frac{\pi\overline{a}}{2}\right)}\frac{0.923 + 0.199\left[1 - \sin\left(\frac{\pi\overline{a}}{2}\right)\right]^4}{\cos\left(\frac{\pi\overline{a}}{2}\right)} \tag{A6}$$

$$F_{\sigma_c}\left(\overline{a}\right) = \sqrt{\frac{2}{\pi\overline{a}}\tan\left(\frac{\pi\overline{a}}{2}\right)}\frac{0.752 + 2.02\overline{a} + 0.37\left[1 - \sin\left(\frac{\pi\overline{a}}{2}\right)\right]^3}{\cos\left(\frac{\pi\overline{a}}{2}\right)} \tag{A7}$$

$$F_{P}\left(\overline{a}\right) = 2\frac{0.46 + 3.06\overline{a} + 0.84\left(1 - \overline{a}\right)^5 + 0.66\overline{a}^2\left(1 - \overline{a}\right)^2}{\left(1 - \overline{a}\right)^{3/2}} \tag{A8}$$
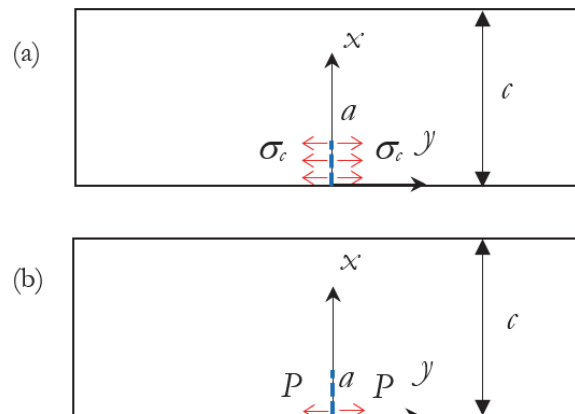

Figure A2: Schematic representation of the considered loadings: (a) cohesive stress acting on the crack length *a*; (b) pair of normal forces *P* applied at the beginning of the crack.

REFERENCES

[1] Hillerborg, A., Modéer, M., Petersson, P.-E. (1976). Analysis of crack formation and crack growth in concrete by means of fracture mechanics and finite elements, Cem. Concr. Res., 6(6), pp. 773–781, DOI: 10.1016/0008-8846(76)90007-7.

[2] Needleman, A. (1990).An analysis of decohesion along an imperfect interface. Non-Linear Fracture, Dordrecht, Springer Netherlands, pp. 21–40.

[3] Leguillon, D. (2002). Strength or toughness? A criterion for crack onset at a notch, Eur. J. Mech. - A/Solids, 21(1), pp. 61–72, DOI: 10.1016/S0997-7538(01)01184-6.

[4] Cornetti, P., Pugno, N., Carpinteri, A., Taylor, D. (2006). Finite fracture mechanics: A coupled stress and energy failure criterion, Eng. Fract. Mech., 73(14), pp. 2021–2033, DOI: 10.1016/j.engfracmech.2006.03.010.

[5] Henninger, C., Leguillon, D., Martin, E. (2007). Crack initiation at a V-notch—comparison between a brittle fracture criterion and the Dugdale cohesive model, Comptes Rendus Mécanique, 335(7), pp. 388–393, DOI: 10.1016/j.crme.2007.05.018.

[6] Cornetti, P., Sapora, A. (2019). Penny-shaped cracks by Finite Fracture Mechanics, Int. J. Fract., 219(1), pp. 153–159, DOI: 10.1007/s10704-019-00383-9.

[7] Doitrand, A., Estevez, R., Leguillon, D. (2019). Comparison between cohesive zone and coupled criterion modeling of crack initiation in rhombus hole specimens under quasi-static compression, Theor. Appl. Fract. Mech., 99, pp. 51–59, DOI: 10.1016/j.tafmec.2018.11.007.

[8] Cornetti, P., Sapora, A., Carpinteri, A. (2016). Short cracks and V-notches: Finite Fracture Mechanics vs. Cohesive

Crack Model, Eng. Fract. Mech., 168, pp. 2–12, DOI: 10.1016/j.engfracmech.2015.12.016.

[9] Cornetti, P., Muñoz-Reja, M., Sapora, A., Carpinteri, A. (2019). Finite fracture mechanics and cohesive crack model: Weight functions vs. cohesive laws, Int. J. Solids Struct., 156–157, pp. 126–136, DOI: 10.1016/j.ijsolstr.2018.08.003.

[10] García, I.G., Paggi, M., Mantič, V. (2014). Fiber-size effects on the onset of fiber–matrix debonding under transverse tension: A comparison between cohesive zone and finite fracture mechanics models, Eng. Fract. Mech., 115, pp. 96–110, DOI: 10.1016/j.engfracmech.2013.10.014.

[11] Chao Correas, A., Corrado, M., Sapora, A., Cornetti, P. (2021). Size-effect on the apparent tensile strength of brittle materials with spherical cavities, Theor. Appl. Fract. Mech., 116, pp. 103120, DOI: 10.1016/j.tafmec.2021.103120.

[12] Li, J., Zhang, X.B. (2006). A criterion study for non-singular stress concentrations in brittle or quasi-brittle materials, Eng. Fract. Mech., 73(4), pp. 505–523, DOI: 10.1016/j.engfracmech.2005.09.001.

[13] Doitrand, A., Henry, R., Meille, S. (2021). Brittle material strength and fracture toughness estimation from four-point bending test, J. Theor. Comput. Appl. Mech., DOI: 10.46298/jtcam.6753.

[14] Taylor, D. (2007). The Theory of Critical Distances, Elsevier, Amsterdam.

[15] Carpinteri, A., Cornetti, P., Pugno, N., Sapora, A., Taylor, D. (2008). A finite fracture mechanics approach to structures with sharp V-notches, Eng. Fract. Mech., 75(7), pp. 1736–1752, DOI: 10.1016/j.engfracmech.2007.04.010.

[16] Taylor, D., Kasiri, S., Brazel, E. (2009). The theory of critical distances applied to problems in fracture and fatigue of bone, Frat. Ed Integrità Strutt., 3(10), pp. 12–20, DOI: 10.3221/IGF-ESIS.10.02.

[17] Sapora, A., Torabi, A.R., Etesam, S., Cornetti, P. (2018). Finite Fracture Mechanics crack initiation from a circular hole, Fatigue Fract. Eng. Mater. Struct., 41(7), pp. 1627–1636, DOI: 10.1111/ffe.12801.

[18] Kirsch, G. (1898). Die Theorie der Elastizitat und die Bedurfnisse der Festigkeitslehre, Zantralblatt Verlin Deutscher Ingenieure.

[19] Harris, H.G., Sabnis, G.M., White, R.N. (1966). Small scale direct models of reinforced and prestressed concreate structures, Ithaca, New York.

[20] Lu, C., Danzer, R., Fischer, F.D. (2004). Scaling of fracture strength in ZnO: Effects of pore/grain-size interaction and porosity, J. Eur. Ceram. Soc., 24(14), pp. 3643–3651, DOI: 10.1016/j.jeurceramsoc.2003.12.001.

[21] Negru, R., Marsavina, L., Voiconi, T., Linul, E., Filipescu, H., Belgiu, G. (2015). Application of TCD for brittle fracture of notched PUR materials, Theor. Appl. Fract. Mech., 80, pp. 87–95, DOI: 10.1016/j.tafmec.2015.05.005.

[22] Lampropoulos, A., Nicolaides, D., Paschalis, S., Tsioulou, O. (2021). Experimental and Numerical Investigation on the Size Effect of Ultrahigh-Performance Fibre-Reinforced Concrete (UHFRC), Materials (Basel)., 14(19), pp. 5714, DOI: 10.3390/ma14195714.

[23] Karihaloo, B.L., Nallathambi, P. (1990). Effective crack model for the determination of fracture toughness () of concrete, Eng. Fract. Mech., 35(4–5), pp. 637–465, DOI: 10.1016/0013-7944(90)90146-8.

[24] Yoshimura, H.N., Molisani, A.L., Narita, N.E., Manholetti, J.L.A., Cavenaghi, J.M. (2006). Mechanical Properties and Microstructure of Zinc Oxide Varistor Ceramics, Mater. Sci. Forum, 530–531, pp. 408–413, DOI: 10.4028/www.scientific.net/MSF.530-531.408.

[25] Meille, S., Garboczi, E.J. (2001). Linear elastic properties of 2D and 3D models of porous materials made from elongated objects, Model. Simul. Mater. Sci. Eng., 9(5), pp. 371–390, DOI: 10.1088/0965-0393/9/5/303.

[26] Meille, S. (2001). Étude du comportement mécanique du plâtre pris en relation avec sa microstructure. Institut National des Sciences Appliquées de Lyon.

[27] Sanahuja, J., Dormieux, L., Meille, S., Hellmich, C., Fritsch, A. (2010). Micromechanical Explanation of Elasticity and Strength of Gypsum: From Elongated Anisotropic Crystals to Isotropic Porous Polycrystals, J. Eng. Mech., 136(2), pp. 239–253, DOI: 10.1061/(ASCE)EM.1943-7889.0000072.

[28] Tran, T.K., Tran, N.T., Nguyen, D.L., Kim, D.J., Park, J.K., Ngo, T.T. (2021). Dynamic fracture toughness of ultra-high-performance fiber-reinforced concrete under impact tensile loading, Struct. Concr., 22(3), pp. 1845–1860, DOI: 10.1002/suco.202000379.

[29] Marsavina, L., Linul, E., Voiconi, T., Constantinescu, D.M., Apostol, D.A. (2015). On the crack path under mixed mode loading on PUR foams, Frat. Ed Integrità Strutt., (34), DOI: 10.3221/IGF-ESIS.34.43.

[30] Tan, S.C. (1988). Finite-Width Correction Factors for Anisotropic Plate Containing a Central Opening, J. Compos. Mater., 22(11), pp. 1080–1097, DOI: 10.1177/002199838802201105.

[31] Newman Jr, J.C. (1983). A nonlinear fracture mechanics approach to the growth of small cracks, Proc. AGARD Conf., 328(6).

[32] Chang, J.B., Hudson, C.M. (1981). A Crack-Closure Model for Predicting Fatigue Crack Growth Under Aircraft Spectrum Loading. Methods and Models for Predicting Fatigue Crack Growth Under Random Loading, American Society for Testing and Materials, pp. 53–84.

[33] Newman Jr, J.C. (1971). An improved Method of Collocation for the Stress Analysis of Cracked Plates with Various Shaped Boundaries, NASA Tech. Note D-6376.

[34] Uhl, J., Doitrand, A., Meille, S. (2022). Variability in porous ceramic fracture: Influence of apparent density and critical pores, J. Eur. Ceram. Soc., DOI: 10.1016/j.jeurceramsoc.2022.05.020.

[35] Carpinteri, A., Cornetti, P., Sapora, A. (2011). Brittle failures at rounded V-notches: a finite fracture mechanics approach, Int. J. Fract., 172(1), pp. 1–8, DOI: 10.1007/s10704-011-9640-8.

[36] Tada, H., Paris, P.C., Irwin, G.R. (2000). The Stress Analysis of Cracks Handbook, Third Edition, ASME Press, New York.

[37] Williams, T.N., Newman Jr, J.C., Gullett, P.M. (2011). Crack-surface displacements for cracks emanating from a circular hole under various loading conditions, Fatigue Fract. Eng. Mater. Struct., 34(4), pp. 250–259, DOI: 10.1111/j.1460-2695.2010.01512.x.